Impact of silica fume, fly ash, and metakaolin on the thickness and strength of the ITZ in concrete

V. Nežerka[a,*], P. Bílý[a], V. Hrbek[a], J. Fládr[a]

[a]*Faculty of Civil Engineering, Czech Technical University in Prague, Thákurova 7, 166 29 Praha 6, Czech Republic*

Abstract

The interfacial transition zone (ITZ) has a major detrimental impact on the structural performance of concrete. This negative impact can be modulated by introducing mineral admixtures to a concrete mix, which fill the excessive voids within ITZ and react with portlandite to form more compact products. The approach described here, consisting of characterization of phases and micromechanical modeling, enabled assessment of the effect of silica fume, fly ash, and metakaolin on ITZ thickness and strength. The proposed model was based on the Mori-Tanaka scheme coupled with an estimation of deviatoric stress within ITZ. This study suggests that silica fume is efficient in reducing ITZ thickness, while the addition of fly ash more significantly contributes to ITZ strength. Moderate replacements of Portland cement for silica fume or fly ash, up to 20%, can positively influence concrete performance; in case of metakaolin, replacement up to 10% is recommended.

Keywords: Concrete, ITZ, Strength, Silica fume, Fly ash, Metakaolin

*Corresponding author

Email address: vaclav.nezerka@fsv.cvut.cz (V. Nežerka)

Nomenclature

w/b	Water-to-binder ratio
m_c	Cement mass
m_{SCM}	Mass of supplementary cementitious materials
p_{tot}	Total porosity
$\mathcal{L}$	Length scale
r	Phase index
δ	Sub-phase index
$c^{\mathcal{L},(r)}$	volumetric fraction of a phase r at a scale $\mathcal{L}$
$R^{(\mathcal{L},(r),\delta)}$	Mean radius of spherical inclusions representing a sub-phase δ of a phase r at a scale $\mathcal{L}$
$t^{III,(2)}$	ITZ thickness
$E^{\mathcal{L},(r)}$	Young's modulus of a phase r at a scale $\mathcal{L}$
$\nu^{(r)}$	Poisson's ratio of a phase r
$K^{(r)}$	Bulk modulus of a phase r
$G^{(r)}$	Shear modulus of a phase r
$\mathcal{N}_{E^{\mathcal{L},(r)}}$	Normal distribution of Young's moduli for a phase r at a scale $\mathcal{L}$
$\bar{X}_{E^{\mathcal{L},(r)}}$	Mean of Young's moduli for a phase r at a scale $\mathcal{L}$
$s_{E^{\mathcal{L},(r)}}$	Standard deviation of Young's moduli for a phase r at a scale $\mathcal{L}$
$\bar{X}_{c^{\mathcal{L},(r)}}$	Mean of volumetric fractions for a phase r at a scale $\mathcal{L}$
$\boldsymbol{\varepsilon}$	Macroscopic strain
$\boldsymbol{\sigma}$	Macroscopic stress
$\boldsymbol{\varepsilon}^{(r)}$	Strain in a phase r
$\boldsymbol{\varepsilon}^{(r)}$	Strain in a phase r
$\mathbf{A}_{\text{dil}}^{(r)}$	Dilute concentration factor for a phase r
$\mathbf{A}_{\text{dil,V}}^{(r)}$	Volumetric projection of a concentration factor for a phase r
$\mathbf{A}_{\text{dil,D}}^{(r)}$	Deviatoric projection of a concentration factor for a phase r
$\mathbf{A}_{\text{MT}}$	Mori-Tanaka concentration factor

Nomenclature

$\mathbf{I}$	Identity matrix
$\mathbf{I}_{\mathrm{V}}$	Volumetric projection matrix
$\mathbf{I}_{\mathrm{D}}$	Deviatoric projection matrix
$\alpha^{(0)}$	Eshelby volumetric factor for spherical inclusions
$\beta^{(0)}$	Eshelby deviatoric factor for spherical inclusions
Q_{11}^1, Q_{11}^2, A_1, A_2, B_1, B_2	Auxiliary factors for coated inclusion derived by Herve and Zaoui [1]
$\mathbf{L}_{\mathrm{eff}}$	Effective (macroscopic) stiffness matrix
K_{eff}	Effective (macroscopic) bulk modulus
G_{eff}	Effective (macroscopic) shear modulus
E_{eff}	Effective (macroscopic) Young's modulus
$f_{\mathrm{c,eff}}$	Effective (macroscopic) compressive strength of concrete
$\boldsymbol{\sigma}^{III,(2,\delta)}$	Stress in individual sub-phases δ of the ITZ
$f_{\mathrm{dev}}^{III,(2,\delta)}$	Deviatoric stress in individual sub-phases δ of the ITZ
$J_2^{(III,2,\delta)}$	Second deviatoric stress invariant for individual sub-phases δ of the ITZ
E_{meas}	Mean of elastic stiffness measurements on macroscopic specimens
$f_{\mathrm{c,meas}}$	Mean value of macroscopically measured strengths on concrete specimens subjected to uniaxial compression
ϵ_E	Error in the effective Young's modulus prediction
$\epsilon_{f_{\mathrm{c}}}$	Error in the effective compressive strength prediction

1. Introduction

The structural performance of concrete depends significantly on the type and quality of aggregates, the properties of the cementitious matrix, and the ITZ between these two components. The ITZ is generally considered to be the weakest link in this performance chain [2, 3], particularly in

terms of fracture behavior [4–6], because the first cracks due to excessive loading usually appear in the vicinity of aggregates [7–12]. Even though the ITZ has a dominant effect on the tensile strength of concrete, its influence on compressive strength is also significant [4, 13, 14]. In the work of Mitsui et al. [13], for example, the performance of mortars having three different ITZ thicknesses were compared; they found that the thinner the ITZ, the higher the tensile and compressive strengths (up to 50%). ITZ strength is also a crucial factor in determining the structural performance of fiber-reinforced cementitious composites (FRC) [15–18]. Bentur et al. [16] concluded that this is because of the large surface area of reinforcement fibers in FRC. These reasons have led to a growing interest in the mechanisms of ITZ formation and particularly in reducing its negative impact on the performance of cementitious composites.

Several authors have employed electron microscopy [4, 19–22] to study and quantify microstructural gradients across ITZs. Their studies have provided valuable information microstructures and morphologies. ITZs are more porous than the bulk cement matrix and contain portlandite crystals with a preferential orientation and highly porous hydration products such as ettringite [22–25]. In cement mortars studied by Scrivener et al. [25], the difference between the porosity of a bulk matrix and the ITZ after 28 days of hardening reached up to 30%. The distribution of Young's modulus and hardness across ITZs was assessed using nanoindentation [26–28], which revealed for strengthening using mineral admixtures. The two major mechanisms responsible for ITZ enhancement are (1) pozzolanic reactions that transform portlandite in the vicinity of aggregate into more stable and stronger calcium-silicate-hydrates (C-S-H) and (2) filling of excessive pores within an ITZ with microscopic particles. Most mineral admixtures, collectively referred to as supplementary cementitious materials (SCMs), are industrial by-products considered to be ecologically burdensome. Hence, their use can, besides minimizing the adverse effects of ITZs on concrete, contribute to more sustainable structures [29–35].

To investigate the impact of selected SCMs on ITZ, a holistic approach consisting of micromechanical characterization of phases, micromechanical modeling, and macroscopic testing was employed in this study to estimate ITZ thickness and strength in concrete samples containing silica fume, fly ash, and metakaolin in various concentrations. Silica fume was chosen for its ability to

make the concrete matrix more compact [36–38], and for its ability to strengthen an ITZ by reducing its local porosity and react with portlandite [39–42]. Similar outcomes were expected with another SCM, fly ash. The addition of this industrial by-product can increase concrete strength and fracture toughness [43, 44] via both microfilling and pozzolanic activity. Fly ash, unlike silica fumes in some cases, does not contribute toalkali-silica reactions in concrete [45, 46]. The last SCM examined, metakaolin, is not an industrial by-product, but is manufactured under carefully controlled conditions [47], obtained by calcination of kaolinitic clay. Because of the high silica and alumina content in metakaolin [48] the rate of pozzolanic reactions and the consumption of portlandite is superior compared to silica fume or fly ash. Metakaolin contributes to densification, lowers creep and shrinkage, and increases resistance to deicing chemicals [49–51].

The proposed micromechanical model enabling estimation of macrocopic strength and stiffness builds upon our previous efforts and the work of other authors who have investigated the role of phases in cementitious materials at the scale of C-S-H gel [52–55] up to the scale of aggregate [56–61]. This strategy was enriched with probabilistic modeling of individual phases via Monte Carlo simulations that required an extensive experimental program consisting of both microscopic and macroscopic tests. The enriched model allowed us to evaluate the effect of the three types of SCMs on ITZ thickness and strength of ITZ around aggregates and to establish suitable Portland cement replacements, considering the negative impact of weak and thick ITZs on the strength and durability of concrete [62–64].

2. Materials and methods

2.1. Materials and samples

The study examined 10 different concrete mixes containing different amounts of SCMs and reinforced with an aggregate of the same type, grading, and concentration. Ordinary Portland cement (referred to as PC) CEM I/42.5R (EN 197-1:2001 [65]) was blended with the following SCMs: (1) silica fume Stachesil S (SF), (2) fly ash produced by the coal-fired Tušimice power plant (FA), and (3) metakaolin Mefisto L05 (MK) produced by claystone grinding and burning.

Besides the reference material (R), mixes with 10%, 20%, and 30% replacements of cement mass by SCMs were examined. Table 1 provides the composition of all mixes. The percentages

of SCM replacement were based on previous studies [66–70]. The effective water-to-binder ratio $w/b = 0.26$ was kept constant for all mixes. The amount of water needed [kg/m^3] was calculated as [71]

$$m_w = \frac{w/b}{m_c + k\, m_{SCM}}, \tag{1}$$

where m_c and m_{SCM} are the mass of cement and SCM per m^3 of a concrete mix. The k-value was determined based on recommendations in EN 206 [72] as 2.0 for SF, 0.4 for FA, and 1.0 for MK. This low w/b ensured low porosity in the prepared samples (Table 2).

Table 1: Composition of mixes prepared; amount of individual components expressed in kg/m^3.

Mix	PC	SCM			Water	Aggregate			Superplasticizer
		SF	FA	MK		0/4 mm	4/8 mm	8/16 mm	
R	800	–	–	–	210	730	390	320	25
S10	720	80	–	–	231	730	390	320	33
S20	640	160	–	–	252	730	390	320	33
S30	560	240	–	–	273	730	390	320	33
F10	720	–	80	–	197	730	390	320	34
F20	640	–	160	–	185	730	390	320	32
F30	560	–	240	–	172	730	390	320	30
M10	720	–	–	80	210	730	390	320	30
M20	640	–	–	160	210	730	390	320	30
M30	560	–	–	240	210	730	390	320	30

Table 2: Total porosity p_{tot}; averages from six measurements carried out according to EN 480-11 [73] using an automated RapidAir 457 system.

R	S10	S20	S30	A10	A20	A30	M10	M20	M30
10.13	8.27	7.86	7.38	9.08	8.48	8.45	10.76	9.26	10.02

The chemical composition of PC and SCMs was determined by X-ray fluorescence spectroscopy (XRF) using a Spectro Xepos spectrometer equipped with 50 W/60 kV X-ray tube.

Table 3 presents a list of identifiable oxides. Based on the ratio of CaO and SiO_2, it can be assumed that the clinker in PC contained mostly C_3S, lower amounts of C_2S, and less than 5 wt% aluminosilicates. SF is an amorphous polymorph of silicon dioxide; thus, high SiO_2 content was expected. The high content of amorphous SiO_2 in FA is provided by the soluble glassy components that are chemically activated in alkaline environment [74]. The same applies to metakaolin, also rich in Al_2O_3 and exhibiting high pozzolanic activity [48, 75].

Table 3: Chemical composition of PC and SCMs; most important oxides and loss on ignition (LOI) identified by the XRF.

	PC	SF	FA	MK
	wt% ($\pm$0.5%)			
CaO	64.2	1.50	4.20	0.00
SiO_2	19.5	92.1	48.8	54.1
Al_2O_3	4.70	0.00	24.2	40.1
Fe_2O_3	3.20	0.41	12.5	1.10
SO_3	3.20	0.00	1.20	0.00
MgO	1.30	0.30	0.70	0.00
K_2O	0.78	0.69	1.40	0.80
TiO_2	0.00	0.00	1.40	1.80
LOI	3.20	5.00	5.53	2.10

A Malvern Mastersizer 3000 laser diffraction particle size analyzer was used to determine the particle size distribution curves for PC and SCMs; the basalt aggregate grading was determined by sieving (Table 5). Distribution curves are provided in Figure 1. Both the distribution curves and size characteristics summarized in Table 4 show that the particle size distribution of PC was shifted towards larger diameters compared to the fine-grained SCMs. Notably, the specific surface area of SF and MK is about 50$\times$ larger than that of PC and FA, which increases their reactivities.

When preparing the concrete mixes, the aggregate was first homogenized. PC was then added, followed by individual SCMs and water containing a Stachement superplasticizer. A standard laboratory mixer at 30 rpm was used. The concrete samples were cast into molds, compacted

Table 4: Size characteristics and bulk density of PC and SCMs.

	PC	SF	FA	MK
Size distribution, 50^{th} percentile [µm]	9.11	2.92	5.89	2.15
Size distribution, 90^{th} percentile [µm]	34.06	6.74	124.35	7.50
Specific surface area [m^2/g]	0.37	15.0	0.25	12.7
Bulk density [kg/m^3]	3100	2400	2000	2300

Table 5: Aggregate grading.

Sieve size [mm]	0	0.0625	0.125	0.25	0.5	1.0	2.0	4.0	8.0	16.0
Passing [%]	0	2.08	3.51	5.40	9.13	16.45	29.74	52.50	78.88	100.00

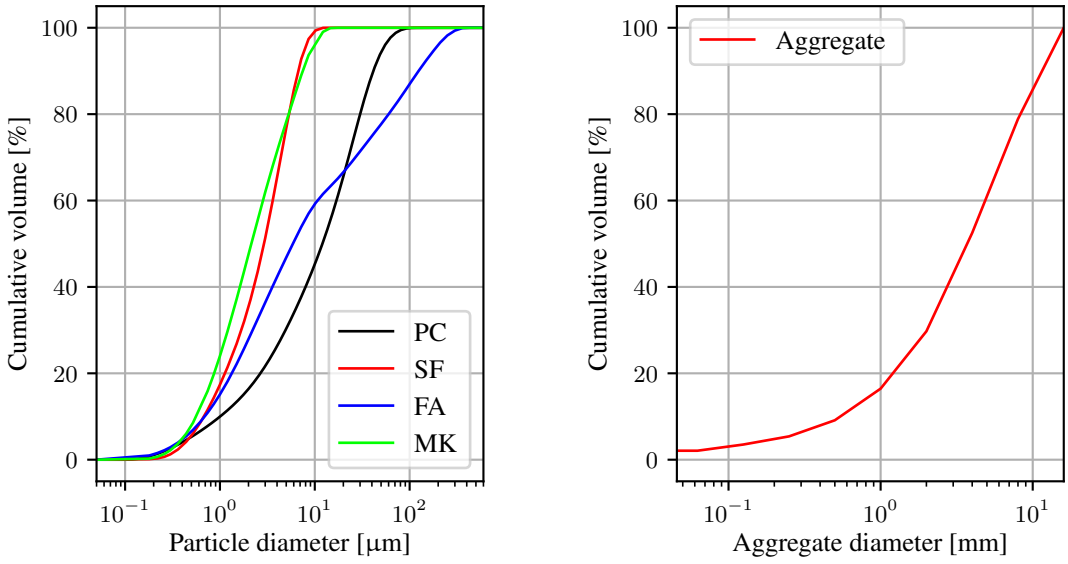

Figure 1: Particle size distribution curves of the used PC and SCM (left) and for the aggregate (right).

during casting, and demolded after 24 hours. Curing was executed in standard atmospheric air at 22±1 °C with a relative humidity of 90±2% for 28 days.

Cylinders (diameter: 100 mm, height: 200 mm) were used for the assessment of Young's modulus. For compressive strength testing, 100 mm cubes were cast. Six specimens represented each mix for both specimen geometries. Each batch was represented by three cylindrical specimens (diameter: 25 mm) for examination with microscopy and nanoindentation. Representative specimens were cut into 15 mm thick slices and polished on an MD-Piano grinding plate using 1200, 2000, and 4000 grain/cm^2 grits under 0.25 N compression and were cleaned with ethanol after each step using an ultrasound cleaner.

2.2. Microstructure investigation

2.2.1. Morphological and chemical analyses

The polished samples were coated with a 20 nm carbon layer to increase electric conductivity and studied by electron microscopy (SEM) using a FEG-SEM Merlin Zeiss microscope. SEM analysis in backscattered electron microscopy (BSE) mode allowed for highlighting phases at required scales. Since grayscale intensity in a BSE image depends on atomic mass [76], individual phases could be identified using an in-house software PyPAIS [77] based on intensity and entropy thresholding (Figure 2). An assessment of texture roughness via entropy calculation was needed for distinguishing several phases having the same grayscale intensity such as smooth SiO_2 and rough C-S-H gel.

2.2.2. Nanoindentation

Stiffness mapping within the microstructure was accomplished using a nanohardness tester (a Ti 750 Hysitron equipped with a Berkovich diamond tip). The indentation on a grid with 10 μm spacing was displacement-controlled to reach a maximum depth of 150 nm and held for a period of 60 s. Such an approach was addressed to eliminate creep bias [78–80]. The Young's modulus for each of the 441 indents per sample was determined from the load-displacement diagram recorded during 5 s unloading using the Oliver and Pharr method [81, 82]. There were 4 sections cut from the core of the cylindrical specimens representing each mix, yielding 1,764 indents per

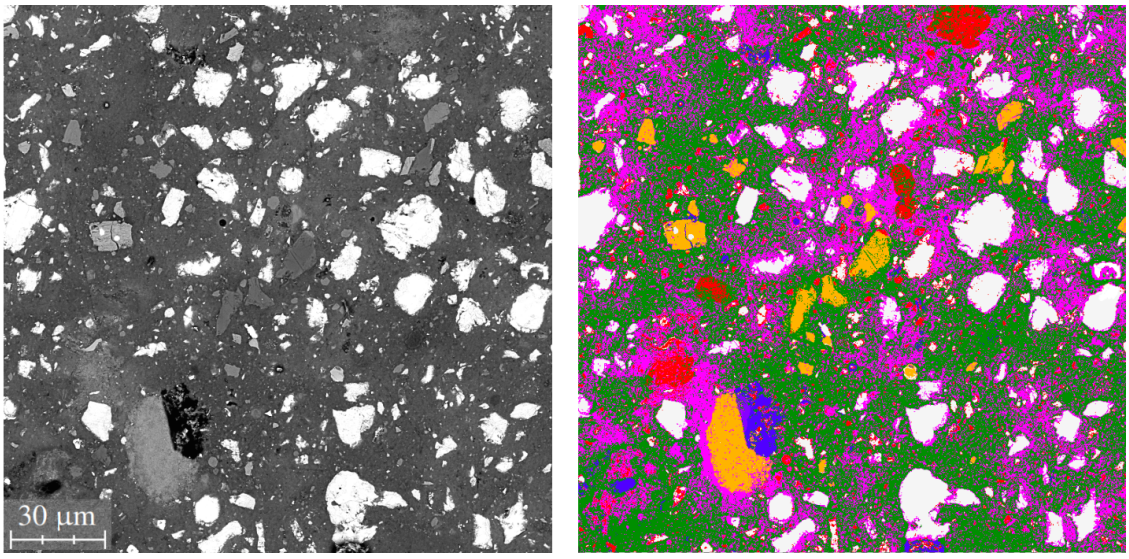

Figure 2: Identification of phases (right) on a M20 sample from a BSE image under 300× magnification (left). Clinker is highlighted in white; portlandite, red; HD C-S-H gel, pink; LD C-S-H gel, green; metakaolin, yellow; and pores, blue.

mix for identification of phases using spectral deconvolution [83, 84]. Attention was paid to the identifying of ITZs; because of their complex morphologies, only their stiffness was assessed with nanoindentation; thickness was estimated using micromechanical modeling (Section 3).

2.3. Testing of macroscopic stiffness and strength

The Young's modulus of macroscopic specimens was tested on the cylindrical specimens using the ultrasonic pulse velocity method following the procedure described in EN 12504-4 [85]. Destructive testing for the assessment of the compressive strength was carried out according to EN 12390-3 [86] using a servo-hydraulic loading frame (EU 2000D by INOVA Praha) with a 2500 kN maximum loading capacity. The loading of specimens was force-controlled at a rate of 5 kN/s. Detailed information on the macroscopic testing of the concrete mixes is presented in the paper by Bílý et al. [87].

3. Modeling

The development of the model was largely inspired by previous works dealing with micromechanical modeling of lime-based mortars [57] and pastes containing waste marble powder [58],

both building upon studies by Pichler and Hellmich [56] and Vorel et. al [88], which utilized a Mori-Tanaka homogenization scheme [89, 90] at multiple scales. Even though not primarily developed for cohesive materials, a criterion based on the von Mises J_2 invariant was selected for strength upscaling based on previous experience [57, 58] and the findings of other authors [91, 92]. Because of its insensitivity to hydrostatic pressure, employing the von Mises criterion makes sense in low confinements such as during uniaxial compression tests.

3.1. Model description

The proposed micromechanical model of concrete containing SCM operates at three length scales. At each scale, $\mathcal{L} = I, II, III$, there is a representative volume element (RVE) composed of m phases indexed by r. The matrix for each scale is represented by $r = 0$ and indices $r = 1, ..., m$ refer to spherical heterogeneities.

At the microscopic scale ($\mathcal{L} = I$), a matrix of low-density C-S-H gel (LD C-S-H) containing high-density C-S-H (HD C-S-H) inclusions is assumed. Non-hydrated clinker, portlandite, and voids are embedded in the homogenized C-S-H matrix at the mesoscale ($\mathcal{L} = II$). At the macroscopic scale ($\mathcal{L} = III$), the presence of stiff aggregate surrounded by ITZs is assumed and modeled as spherical shells (Figure 3). All the phases are assumed to be homogeneous and isotropic; such a simplification of morphology brings computational benefits without significant sacrifice of accuracy [55, 93]. The onset of cracking due to excessive compression is expected to take place within the ITZs, which is in agreement with observations [7–10] and micromechanical modeling of concrete failure mechanisms due to compression-dominated loading [12, 94, 95].

For detailed information on the development of the model, see our preceding papers [57, 58, 96]. Here, the model is extended to incorporate probability distributions of Young's moduli for individual phases $E^{\mathcal{L},(r)}$. By assuming input variables independent one another, Monte Carlo simulations utilizing a random selection following the normal distribution $\mathcal{N}_{E^{\mathcal{L},(r)}}(\bar{X}_{E^{\mathcal{L},(r)}}, s_{E^{\mathcal{L},(r)}})$ could be employed. These distributions were defined based on the experimentally obtained mean values $\bar{X}_{E^{\mathcal{L},(r)}}$ and standard deviations $s_{E^{\mathcal{L},(r)}}$. Because the volumetric fractions $c^{\mathcal{L},(r)}$ exhibited very small variations and cannot be considered completely independent of one another, the measured mean $\bar{X}_{c^{\mathcal{L},(r)}}$ was adopted in modeling as a deterministic parameter $c^{\mathcal{L},(r)}$. The volumetric fractions were

recalculated in such a way to preserve the experimentally obtained ratio and yield

$$\sum_{r=0}^{m} c^{\mathcal{L},(r)} = 1.0 \tag{2}$$

for each $\mathcal{L}$ [97]. At $\mathcal{L} = III$, the volumetric fraction of the ITZ, $c^{\mathcal{III},(2)}$, which was dependent on ITZ thickness, was subtracted from the volumetric fraction of the cement paste matrix, $c^{\mathcal{III},(0)}$.

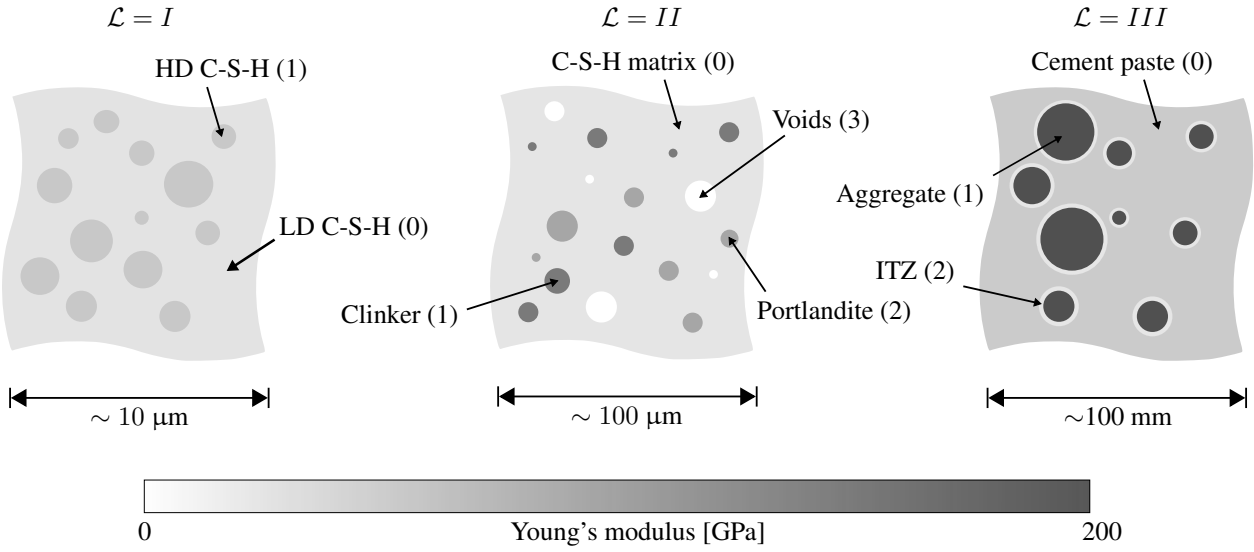

Figure 3: Homogenization scheme; for description of individual phases denoted by numbers in parentheses see Table 6.

3.1.1. Elasticity homogenization

In the Mori-Tanaka scheme, the strain in individual phases is related to the macroscopic strain, $\boldsymbol{\varepsilon}$, using dilute concentration factors $\mathbf{A}_{\text{dil}}^{(r)}$ as $\boldsymbol{\varepsilon}^{(r)} = \mathbf{A}_{\text{dil}}^{(r)}\boldsymbol{\varepsilon}^{(0)}$, where $\boldsymbol{\varepsilon}^{(0)}$ is the strain within the matrix found as

$$\boldsymbol{\varepsilon}^{(0)} = \mathbf{A}_{\text{MT}}\boldsymbol{\varepsilon}, \tag{3}$$

in which the Mori-Tanaka strain concentration factor $\mathbf{A}_{\text{MT}}$ is provided as

$$\mathbf{A}_{\text{MT}} = \left(c^{(0)}\mathbf{I} + \sum_{r=1}^{m} c^{(r)}\mathbf{A}_{\text{dil}}^{(r)} \right)^{-1}, \tag{4}$$

where $\mathbf{I}$ is the identity matrix.

Because of the assumed isotropy, the effective stiffness can be expressed in terms of the effective bulk and shear moduli as

$$K_{\text{eff}} = \frac{c^{(0)}K^{(0)} + \sum_{r=1}^{m} c^{(r)}K^{(r)}A^{(r)}_{\text{dil,V}}}{c^{(0)} + \sum_{r=1}^{m} c^{(r)}A^{(r)}_{\text{dil,V}}}, \qquad G_{\text{eff}} = \frac{c^{(0)}G^{(0)} + \sum_{r=1}^{m} c^{(r)}G^{(r)}A^{(r)}_{\text{dil,D}}}{c^{(0)} + \sum_{r=1}^{m} c^{(r)}A^{(r)}_{\text{dil,D}}}. \tag{5}$$

Knowing the effective bulk and shear moduli, one can calculate all elastic parameters [98], e.g. Young's modulus E_{eff}, or assemble the effective stiffness matrix for an isotropic material $\mathbf{L}_{\text{eff}}$.

The volumetric and deviatoric components of the dilute concentration factors, $A^{(r)}_{\text{dil,V}}$ and $A^{(r)}_{\text{dil,D}}$, can be expressed as

$$\mathbf{A}^{(r)}_{\text{dil}} = A^{(r)}_{\text{dil,V}}\mathbf{I}_{\text{V}} + A^{(r)}_{\text{dil,D}}\mathbf{I}_{\text{D}}, r = 1, ..., m, \tag{6}$$

where $\mathbf{I}_{\text{V}}$ and $\mathbf{I}_{\text{D}}$ are orthogonal projections to the volumetric and deviatoric components, respectively.

Analogically to Eq. (5), the volumetric and deviatoric components of the dilute concentration factors for spherical inclusions, following the work of [99], can be decomposed to

$$A^{(r)}_{\text{dil,V}} = \frac{K^{(0)}}{K^{(0)} + \alpha^{(0)}\left(K^{(r)} - K^{(0)}\right)}, \qquad A^{(r)}_{\text{dil,D}} = \frac{G^{(0)}}{G^{(0)} + \beta^{(0)}\left(G^{(r)} - G^{(0)}\right)}, \tag{7}$$

where $\alpha^{(0)}$ and $\beta^{(0)}$ depend purely on the Poisson's ratio of the C-S-H matrix, $\nu^{(0)}$, as

$$\alpha^{(0)} = \frac{1 + \nu^{(0)}}{3(1 + \nu^{(0)})}, \qquad \beta^{(0)} = \frac{2(4 - 5\nu^{(0)})}{15(1 - \nu^{(0)})}. \tag{8}$$

The expressions for the dilute concentrations factors of particles coated by spherical shells were derived by Herve and Zaoui [1]. To respect the sensitivity of the model to aggregate grading, the aggregate and the ITZ had to be split into δ sub-phases corresponding to individual grading intervals denoted by indices $(III, (1, \delta))$ and $(III, (2, \delta))$, respectively. The dilute concentration factors of the coated inclusions and their coating depend on their outer radii, $R^{(III,(1),\delta)}$ and $R^{III,(2,\delta)}$, and Poisson's ratios, $\nu^{III,(1)}$ and $\nu^{III,(2)}$, as follows

$$A^{III,(1,\delta)}_{\text{dil,V}} = \frac{1}{Q^2_{11}}, \tag{9}$$

$$A_{\mathrm{dil,V}}^{III,(2,\delta)} = \frac{Q_{11}^1}{Q_{11}^2} \tag{10}$$

and

$$A_{\mathrm{dil,D}}^{III,(1,\delta)} = A_1 - \frac{21}{5}\frac{{R^{III,(1,\delta)}}^2}{1-2\nu^{III,(1)}}B_1, \tag{11}$$

$$A_{\mathrm{dil,D}}^{III,(2,\delta)} = A_2 - \frac{21}{5}\frac{{R^{III,(2,\delta)}}^5 - {R^{III,(1,\delta)}}^5}{(1-2\nu^{III,(2)})({R^{III,(2,\delta)}}^3 - {R^{III,(1,\delta)}}^3)}B_2, \tag{12}$$

where the auxiliary factors Q_{11}^1, Q_{11}^2, A_1, A_2, B_1, and B_2 are provided, e.g., in the work of Nežerka and Zeman [96, Appendix A].

3.1.2. Compressive strength estimation

To estimate the response of concrete to uniaxial compression, the von Mises failure criterion defined as

$$\sqrt{J_2^{III,(2)}} - \frac{f_{\mathrm{dev}}^{III,(2)}}{\sqrt{3}} = 0, \tag{13}$$

is considered. The resistance of ITZs to the deviatoric stress due to macroscopically applied uniaxial compression is represented by $f_{\mathrm{dev}}^{III,(2,\delta)}$, while the second deviatoric stress invariant in the ITZs, $J_2^{(III,2,\delta)}$, is determined from the average matrix stress, $\boldsymbol{\sigma}^{(0)}$, as

$$J_2^{III,(2,\delta)} = \frac{1}{2}{\boldsymbol{\sigma}^{(0)}}^{\mathrm{T}}\mathbf{I}_{\mathrm{D}}\boldsymbol{\sigma}^{(0)}. \tag{14}$$

The average stress in an ITZ, $\boldsymbol{\sigma}^{(0)}$, is related to the macroscopic stress $\boldsymbol{\sigma}$ via

$$\boldsymbol{\sigma}^{(0)} = \mathbf{L}^{(0)}\mathbf{A}_{\mathrm{dil}}^{III,(2,\delta)}\mathbf{A}_{\mathrm{MT}}\left(\mathbf{L}_{\mathrm{eff}}\right)^{-1}\boldsymbol{\sigma}, \tag{15}$$

where $\mathbf{L}^{(0)}$ and $\mathbf{L}_{\mathrm{eff}}$ are the elastic stiffness matrices for an isotropic material, representing the matrix and the homogenized composite, respectively. The effective compressive strength of concrete, $f_{\mathrm{c,eff}}$, can be found by subjecting the sample to $\boldsymbol{\sigma} = [-f_{\mathrm{c,eff}}, 0, 0, 0, 0, 0]^{\mathrm{T}}$ so that the von Mises condition (Eq. (13)) is satisfied.

Table 6: Modeling assumptions and description of phases; parameters marked with asterisk (*), i.e. ITZ thickness $t^{III,(2)}$ and strength $f_{\text{dev}}^{III,(2)}$, are found by fitting the model outcomes to the results of experimental testing at macro scale.

Phase	$\mathcal{L}$	Parameters	Description
LD C-S-H	I	$c^{I,(0)}, \mathcal{N}_{E^{I,(0)}}, \nu^{I,(0)} = 0.24$ [53]	Matrix at scale I
HD C-S-H	I	$c^{I,(1)}, \mathcal{N}_{E^{I,(1)}}, \nu^{I,(1)} = 0.24$ [53, 100]	Spherical inclusions
C-S-H matrix	II	$c^{II,(0)}, \mathcal{N}_{E^{II,(0)}}, \mathcal{N}_{\nu^{II,(0)}}$	Effective E and ν from $\mathcal{L}$ = I
Portlandite	II	$c^{II,(1)}, \mathcal{N}_{E^{II,(1)}}, \nu^{II,(1)} = 0.31$ [53, 101]	Spherical inclusions
Clinker	II	$c^{II,(2)}, \mathcal{N}_{E^{II,(2)}}, \nu^{II,(2)} = 0.30$ [102, 103]	Spherical inclusions
Voids	II	$c^{II,(3)}, \mathcal{N}_{\nu^{II,(0)}}$	Spherical inclusions
Cement paste	III	$c^{III,(0)}, \mathcal{N}_{E^{III,(0)}}, \mathcal{N}_{\nu^{III,(0)}}$	Effective E and ν from $\mathcal{L}$ = II
Aggregate	III	$c^{III,(1)}, \mathcal{N}_{E^{III,(1)}}, \nu^{III,(1)} = 0.25$ [104], $R^{III,(1)}$	Spherical inclusions coated by an ITZ
ITZ	III	$\mathcal{N}_{E^{III,(2)}}, \mathcal{N}_{\nu^{III,(0)}}, t^{III,(2),*}, f_{\text{dev}}^{III,(2),*}$	Spherical shells around aggregate

3.2. Model inputs

The volumetric fraction for each phase was assessed by image analysis of 6 samples representing each mix. The images were taken under 5× (optical microscope), 100× (BSE-EDS), and 500× (BSE-EDS) magnifications, respectively; Table 7 presents results of this analysis. The Young's modulus of individual phases was assessed by deconvolution of the stiffness distributions from nanoindentation measurements (Table 8). The samples containing SF and MK contained a smaller amount of portlandite, a consequence of their pozzolanic activity. FA supported the clinker reaction because there was a lower concentration of unhydrated clinker in F30. The C-S-H gel exhibited superior quality to the reference material in terms of stiffness in all the samples containing additives. The total porosity (Table 2), was reduced by approximately 10–20% additions of SF and FA and was almost the same in the samples containing MK, compared to the reference sample.

Normal distributions $\mathcal{N}_{E^{\mathcal{L},(r)}}(\bar{X}_{E^{\mathcal{L},(r)}}, s_{E^{\mathcal{L},(r)}})$ of Young's moduli were established based on nanoindentation measurements. By employing Monte Carlo simulations, 18,000 random values of Young's moduli $E^{\mathcal{L},(r)}$ representing each phase were generated following the normal distributions (Figure 4).

Table 7: Mean values $\bar{X}_{c^{\mathcal{L},(r)}}$ and standard deviations $s_{c^{\mathcal{L},(r)}}$ of the volumetric fraction $c^{\mathcal{L},(r)}$ for individual phases r; micropores are not present here and are included within the total porosity (Table 2).

	LD C-S-H		HD C-S-H		Portlandite		Clinker		Aggregate	
	$\bar{X}_{c^{\mathcal{L},(r)}}$	$s_{c^{\mathcal{L},(r)}}$	$\bar{X}_{c^{\mathcal{L},(r)}}$	$s_{c^{\mathcal{L},(r)}}$	$\bar{X}_{c^{\mathcal{L},(r)}}$	$s_{c^{\mathcal{L},(r)}}$	$\bar{X}_{c^{\mathcal{L},(r)}}$	$s_{c^{\mathcal{L},(r)}}$	$\bar{X}_{c^{\mathcal{L},(r)}}$	$s_{c^{\mathcal{L},(r)}}$
R	15.82	0.25	15.43	0.35	6.55	0.15	4.18	0.02	56.52	1.39
S10	16.09	0.42	16.61	0.44	4.07	0.06	5.43	0.16	57.45	2.44
S20	18.30	0.98	14.57	0.17	4.49	0.13	6.48	0.22	55.56	3.31
S30	19.33	0.01	13.74	0.38	5.75	0.20	6.76	0.25	56.33	2.79
F10	19.61	0.31	15.34	0.15	5.77	0.11	6.20	0.18	57.89	2.44
F20	12.25	0.40	13.96	0.71	8.50	0.03	2.93	0.23	60.78	1.88
F30	13.48	0.70	13.79	0.50	8.40	0.05	2.81	0.12	59.18	1.93
M10	18.00	0.21	12.59	0.05	4.65	0.02	6.08	0.18	59.38	1.41
M20	18.94	0.33	12.90	0.62	3.82	0.21	5.50	0.23	61.26	0.98
M30	18.78	0.54	12.93	0.53	3.23	0.16	4.81	0.12	60.78	1.03

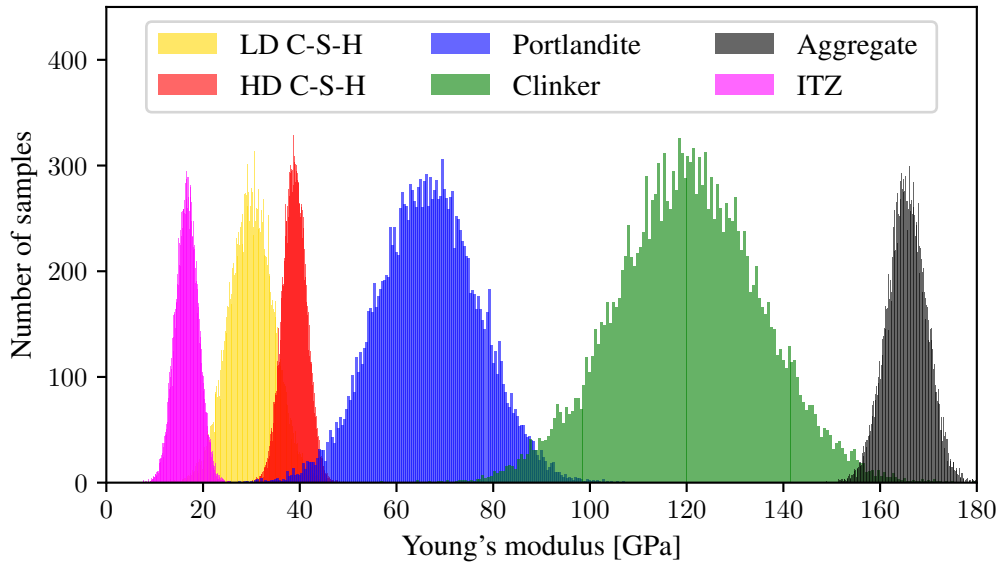

Figure 4: Distribution $\mathcal{N}_{E^{\mathcal{L},(r)}}$ of randomly generated values $E^{\mathcal{L},(r)}$ representing the reference mix without SCMs.

Table 8: Mean values $\bar{X}_{E^{\mathcal{L},(r)}}$ and standard deviations $s_{E^{\mathcal{L},(r)}}$ of the indentation modulus $E^{\mathcal{L},(r)}$ [GPa] for individual phases r.

	LD C-S-H		HD C-S-H		Portlandite		Clinker		Aggregate		ITZ	
	$\bar{X}_{E^{\mathcal{L},(r)}}$	$s_{E^{\mathcal{L},(r)}}$	$\bar{X}_{E^{\mathcal{L},(r)}}$	$s_{E^{\mathcal{L},(r)}}$	$\bar{X}_{E^{\mathcal{L},(r)}}$	$s_{E^{\mathcal{L},(r)}}$	$\bar{X}_{E^{\mathcal{L},(r)}}$	$s_{E^{\mathcal{L},(r)}}$	$\bar{X}_{E^{\mathcal{L},(r)}}$	$s_{E^{\mathcal{L},(r)}}$	$\bar{X}_{E^{\mathcal{L},(r)}}$	$s_{E^{\mathcal{L},(r)}}$
R	31.08	4.65	45.07	2.47	81.60	10.36	128.36	14.99	162.78	4.11	17.34	2.38
S10	32.91	4.16	48.43	5.78	66.55	8.50	122.28	8.50	164.58	8.22	16.82	2.18
S20	33.37	2.92	48.94	4.24	66.12	11.74	135.49	11.74	166.84	7.43	18.47	2.41
S30	34.70	3.17	49.98	3.48	65.82	6.51	132.65	6.51	167.47	14.0	18.87	3.91
F10	33.45	5.89	54.54	7.63	84.92	14.07	142.13	13.34	164.86	4.89	16.74	2.42
F20	34.95	5.36	54.99	6.38	88.63	13.16	140.22	12.42	163.32	7.81	16.48	2.12
F30	35.62	5.87	57.72	6.40	86.17	7.59	127.57	16.85	166.54	8.28	18.80	4.40
M10	34.73	4.82	52.32	8.56	85.36	12.06	135.12	18.01	167.53	5.99	15.38	1.98
M20	35.15	6.28	53.27	8.71	87.88	14.55	141.20	18.85	168.32	6.20	15.54	3.24
M30	35.27	5.69	55.40	6.32	84.79	10.26	138.62	14.42	165.45	7.05	16.01	2.25

ITZ thicknesses $t^{III,(2)}$ were assessed by minimizing the error

$$\epsilon_E = \frac{|E_{\text{eff}} - E_{\text{meas}}|}{E_{\text{meas}}} \times 100 \ \ [\%], \tag{16}$$

where E_{meas} is the mean of elastic stiffness measurements on macroscopic specimens. Analogically, the strength of ITZ $f_{\text{dev}}^{III,(2)}$ was calculated by minimizing

$$\epsilon_{f_c} = \frac{|f_{c,\text{eff}} - f_{c,\text{meas}}|}{f_{c,\text{meas}}} \times 100 \ \ [\%], \tag{17}$$

where $f_{c,\text{meas}}$ represents a mean value of macroscopically measured strengths on concrete specimens subjected to uniaxial compression. Table 9 presents the results of macroscopic testing, along with corresponding estimates of ITZ thickness and strength.

4. Results and discussion

The proposed micromechanical model, despite many adopted simplifications (spherical shape of inclusions, strict separation of phases to three length scales, material homogeneity and isotropy of phases, and onset and localization of damage within an ITZ at $\mathcal{L} = III$) is capable of predicting ITZ strength and stiffness within the limits reported in literature. By minimizing the prediction errors ϵ_E and ϵ_{f_c} (Figure 5), it was possible to find the optimum values of ITZ thickness and strength for each mix. Figure 6 summarizes the results; the relationship between the amount of individual SCMs and ITZ properties is clearly apparent.

Replacement of PC by 10% SF resulted in ITZ thickness reduction up to 25%, while 30% replacement yielded a 65% reduction. This result is in agreement with Rossignolo's [105] SEM-EDX observations, who reported a 36% thickness reduction for the 10% replacement. The lowest replacement also yielded a 5% increase in ITZ strength, while 30% replacement resulted in strength reduction. Our previous purely experimental study [70] that focused on PC replacements up to 80% showed a more than 30% reduction in compressive strength when SF replaced PC at 30% instead of 20%. Therefore, a 20% replacement seems to be a reasonable upper limit.

Replacing PC with FA resulted in ITZ thickness reduction as well as strength enhancement, regardless of the amount of replacement. However, 20% replacements of PC with FA yielded a 37% ITZ thickness reduction and a 22% strength enhancement. The aforementioned study [70]

reported a 15% drop in compressive strength after elevating FA replacement from 20% to 30%, confirming that a 20% replacement is the reasonable amount.

The impact of MK on the ITZ was less positive than for SF and FA additions. Even though a 10% replacement of PC by MK reduced ITZ thickness by 48%, strength was also slightly reduced. A 20% replacement resulted in a 15% ITZ thickness reduction and an 8% strength enhancement, while 30% replacement made the ITZ thicker and weaker.

Table 9: Summary of optimization results.

	Measurements		Calculations		ITZ parameters	
	E_{meas} [GPa]	$f_{\text{c,meas}}$ [MPa]	E_{eff} [GPa]	$f_{\text{c,eff}}$ [MPa]	$t^{III,(2)}$ [µm]	$f_{\text{dev}}^{III,(2)}$ [MPa]
R	44.6±1.24	105.9±1.98	44.6±0.35	105.8±1.08	20.70	179.3
S10	51.3±2.57	109.3±2.84	51.3±1.02	106.0±1.52	15.58	198.5
S20	55.0±4.13	101.3±4.25	55.0±0.25	101.3±1.70	9.27	183.3
S30	55.9±1.23	97.7±6.77	55.9±0.99	97.6±1.27	7.30	177.3
F10	52.1±3.65	106.6±7.85	52.1±1.29	106.8±1.91	17.55	213.6
F20	56.2±2.97	120.8±1.25	56.2±1.04	120.9±1.66	13.21	229.8
F30	56.4±1.73	125.3±2.39	56.4±1.13	125.3±1.63	14.79	224.8
M10	48.7±3.46	108.9±2.92	48.7±1.09	109.0±1.82	10.85	177.3
M20	51.2±1.94	110.3±4.50	51.2±1.10	110.2±1.62	17.15	182.4
M30	47.9±1.87	96.7±4.04	47.9±1.02	96.8±1.30	23.46	165.2

The predicted ITZ thicknesses fall within the range suggested by prior studies: that ITZ thickness should be about 10 µm [63, 106] (for studies suggesting higher values, up to 30 µm, see [107, 108]). The positive impact of SF and FA on an ITZ correlates with other studies, which also reported thickness reduction and increased integrity due to the pozzolanic and microfilling effects of these mineral admixtures based on microstructure observations [24, 109, 110]. The less positive impact of MK on ITZ strength shows agreement with the statistical analysis of the effect of mineral admixtures by Paulon et al. [111]. It is worth mentioning that ITZ properties are notably influenced by w/b, so the amount of kneading water should be carefully considered, see Cwirzen and Penttala [112].

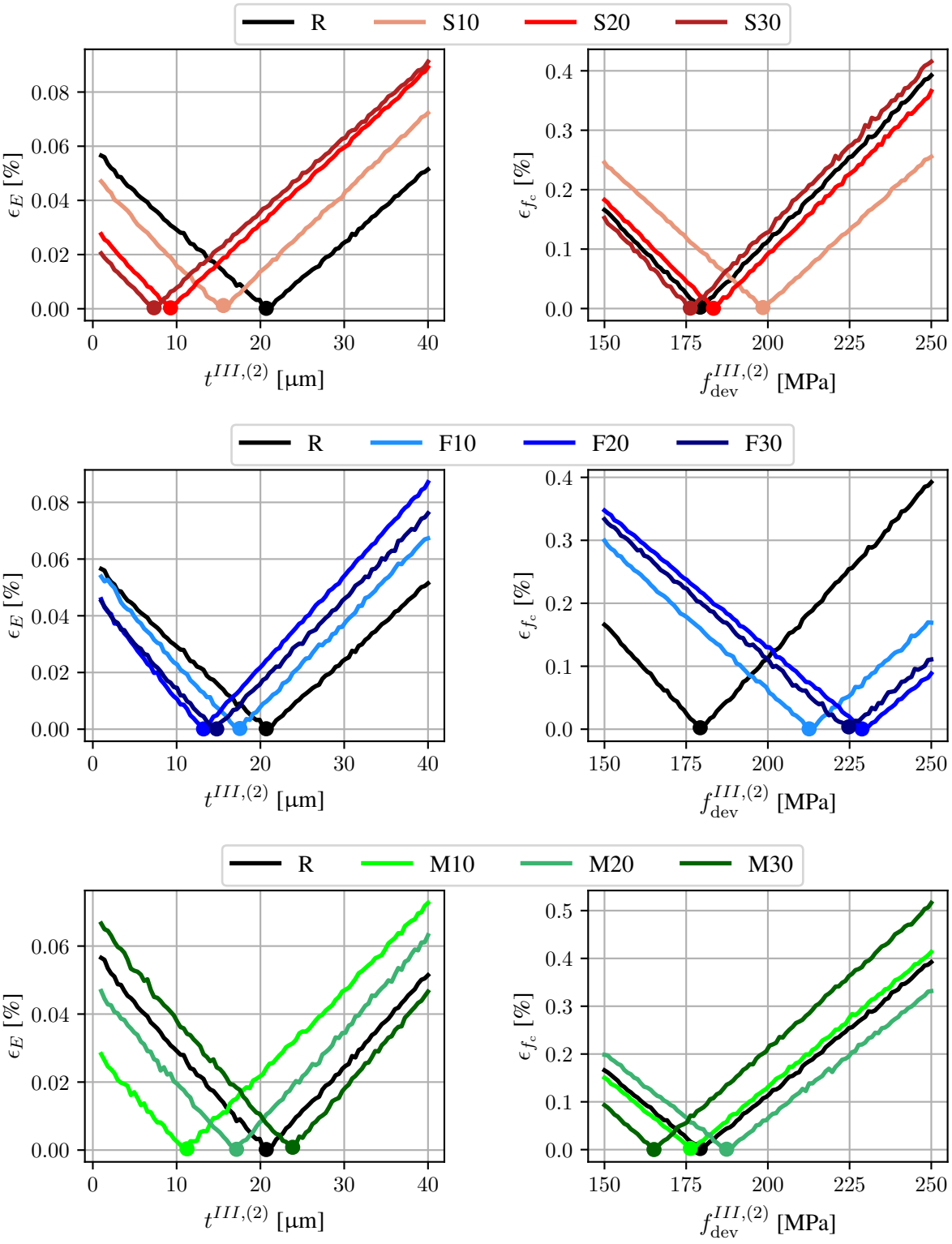

Figure 5: Optimization of ITZ thicknesses $t^{III,(2)}$ and deviatoric strengths $f_{\mathrm{dev}}^{III,(2)}$ by minimizing the differences $|E_{\mathrm{eff}} - E_{\mathrm{meas}}|$ and $|f_{\mathrm{c,eff}} - f_{\mathrm{c,meas}}|$.

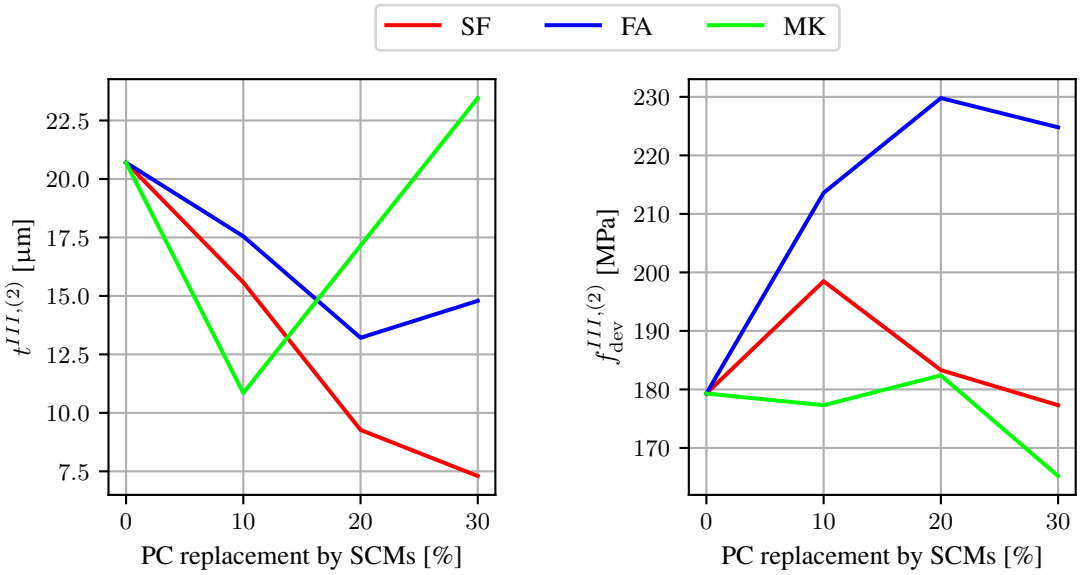

Figure 6: Impact of individual SCMs on ITZ thickness (left) and strength (right).

5. Conclusion

The Mori-Tanaka homogenization scheme and the von Mises failure criterion were selected to estimate the strength and stiffness of cement pastes containing SCMs. This approach was enriched with probabilistic modeling of individual phases via Monte Carlo simulations. By adjusting ITZ thickness and strength, a perfect match to experimentally obtained data was found. This study suggests that the thickness and strength of ITZs around aggregates in concrete can be influenced by replacing a portion of Portland cement in a concrete mix by mineral admixtures such as silica fume, fly ash, or metakaolin.

Due to many simplifications adopted in the micromechanical model, the quantification of ITZ properties cannot be considered exact, but several trends can be observed:

- Addition of secondary cementitious materials can enhance an ITZ by reducing its thickness and increasing its strength.
- Silica fume is more efficient in reducing ITZ thickness than fly ash or metakaolin.
- Fly ash is more efficient for ITZ strengthening than silica fume or metakaolin.

Based on these results, it appears reasonable to replace 10–20% of Portland cement mass in a concrete mix with silica fume or fly ash in order to improve the ITZ around aggregates and produce concrete with superior strength and durability. Metakaolin was not as efficient; only small Portland cement replacements, up to 10%, seem reasonable.

Acknowledgment

The help of Dr. Stephanie Krueger, who provided editorial assistance, is gratefully acknowledged.

Funding. This work was supported by the Czech Science Foundation [grant number GA ČR 17-19463S].

References

[1] E. Herve, A. Zaoui, n-layered inclusion-based micromechanical modelling, International Journal of Engineering Science 31 (1993) 1–10. doi:http://dx.doi.org/10.1016/0020-7225(93)90059-4.

[2] T. Hsu, F. Slate, G. Sturman, G. Winter, Microcracking of plain concrete and the shape of the stress-strain curve, ACI Journal Proceedings 60 (1963) 209–224. doi:10.14359/7852.

[3] S. Shah, S. Chandra, Critical stress, volume change, and microcracking of concrete, ACI Journal Proceedings 65 (1968) 770–780. doi:10.14359/7512.

[4] T. Akçaoğlu, M. Tokyay, T. Çelik, Assessing the ITZ microcracking via scanning electron microscope and its effect on the failure behavior of concrete, Cement and Concrete Research 35 (2005) 358–363. doi:10.1016/j.cemconres.2004.05.042.

[5] I. Merchant, D. Macphee, H. Chandler, R. Henderson, Toughening cement-based materials through the control of interfacial bonding, Cement and Concrete Research 31 (2001) 1873–1880. doi:10.1016/s0008-8846(01)00500-2.

[6] G. Guinea, K. El-Sayed, C. Rocco, M. Elices, J. Planas, The effect of the bond between the matrix and the aggregates on the cracking mechanism and fracture parameters of concrete, Cement and Concrete Research 32 (2002) 1961–1970. doi:10.1016/s0008-8846(02)00902-x.

[7] B. Mobasher, C. Y. Li, Effect of interfacial properties on the crack propagation in cementitious composites, Advanced Cement Based Materials 4 (1996) 93–105. doi:10.1016/s1065-7355(96)90078-4.

[8] P. Simeonov, S. Ahmad, Effect of transition zone on the elastic behavior of cement-based composites, Cement and Concrete Research 25 (1995) 165–176. doi:10.1016/0008-8846(94)00124-h.

[9] M. Saito, M. Kawamura, Resistance of the cement-aggregate interfacial zone to the propagation of cracks, Cement and Concrete Research 16 (1986) 653–661. doi:10.1016/0008-8846(86)90038-4.

[10] G. Giaccio, R. Zerbino, Failure mechanism of concrete, Advanced Cement Based Materials 7 (1998) 41–48. doi:10.1016/s1065-7355(97)00014-x.

[11] S. Zhang, C. Zhang, L. Liao, C. Wang, Numerical study of the effect of ITZ on the failure behaviour of concrete by using particle element modelling, Construction and Building Materials 170 (2018) 776–789. doi:10.1016/j.conbuildmat.2018.03.040.

[12] M. Königsberger, M. Hlobil, B. Delsaute, S. Staquet, C. Hellmich, B. Pichler, Hydrate failure in ITZ governs concrete strength: A micro-to-macro validated engineering mechanics model, Cement and Concrete Research 103 (2018) 77–94. doi:10.1016/j.cemconres.2017.10.002.

[13] K. Mitsui, Z. Li, D. Lange, Relationship between microstructure and mechanical properties of paste-aggregate interface, ACI Materials Journal 91 (1994) 30–39. doi:10.14359/4447.

[14] M. Husem, The effects of bond strengths between lightweight and ordinary aggregate-mortar, aggregate-cement paste on the mechanical properties of concrete, Materials Science and Engineering: A 363 (2003) 152–158. doi:10.1016/s0921-5093(03)00595-1.

[15] V. C. Li, Y. Wang, S. Backer, A micromechanical model of tension-softening and bridging toughening of short random fiber reinforced brittle matrix composites, Journal of the Mechanics and Physics of Solids 39 (1991) 607–625. doi:10.1016/0022-5096(91)90043-n.

[16] A. Bentur, M. G. Alexander, A review of the work of the RILEM TC 159-ETC: Engineering of the interfacial transition zone in cementitious composites, Materials and Structures 33 (2000) 82–87. doi:10.1007/bf02484160.

[17] J. Trejbal, L. Kopecký, P. Tesárek, J. Fládr, J. Antoš, M. Somr, V. Nežerka, Impact of surface plasma treatment on the performance of PET fiber reinforcement in cementitious composites, Cement and Concrete Research 89 (2016) 276–287. doi:10.1016/j.cemconres.2016.08.018.

[18] J. Trejbal, Mechanical properties of lime-based mortars reinforced with plasma treated glass fibers, Construction and Building Materials 190 (2018) 929–938. doi:10.1016/j.conbuildmat.2018.09.175.

[19] M. Mouret, A. Bascoul, G. Escadeillas, Microstructural features of concrete in relation to initial temperature—SEM and ESEM characterization, Cement and Concrete Research 29 (1999) 369–375. doi:10.1016/s0008-8846(98)00160-4.

[20] L. Gatty, S. Bonnamy, A. Feylessoufi, C. Clinard, P. Richard, H. V. Damme, A transmission electron microscopy study of interfaces and matrix homogeneity in ultra-high-performance cement-based materials 36 (2001) 4013–4026. doi:10.1023/a:1017938725748.

[21] S. Diamond, Considerations in image analysis as applied to investigations of the ITZ

in concrete, Cement and Concrete Composites 23 (2001) 171–178. doi:10.1016/s0958-9465(00)00085-8.

[22] K. L. Scrivener, Backscattered electron imaging of cementitious microstructures: understanding and quantification, Cement and Concrete Composites 26 (2004) 935–945. doi:10.1016/j.cemconcomp.2004.02.029.

[23] K. O. Kjellsen, O. H. Wallevik, L. Fjllberg, Microstructure and microchemistry of the paste—aggregate interfacial transition zone of high-performance concrete, Advances in Cement Research 10 (1998) 33–40. doi:10.1680/adcr.1998.10.1.33.

[24] M. Nili, A. Ehsani, Investigating the effect of the cement paste and transition zone on strength development of concrete containing nanosilica and silica fume, Materials & Design 75 (2015) 174–183. doi:10.1016/j.matdes.2015.03.024.

[25] K. L. Scrivener, A. K. Crumbie, P. Laugesen, The interfacial transition zone (ITZ) between cement paste and aggregate in concrete, Interface Science 12 (2004) 411–421. doi:10.1023/b:ints.0000042339.92990.4c.

[26] M. J. DeJong, F.-J. Ulm, The nanogranular behavior of C-S-H at elevated temperatures (up to 700°c), Cement and Concrete Research 37 (2007) 1–12. doi:10.1016/j.cemconres.2006.09.006.

[27] P. Mondal, S. P. Shah, L. Marks, A reliable technique to determine the local mechanical properties at the nanoscale for cementitious materials, Cement and Concrete Research 37 (2007) 1440–1444. doi:10.1016/j.cemconres.2007.07.001.

[28] P. Mondal, S. Shah, L. Marks, Nanoscale characterization of cementitious materials, ACI Materials Journal 105. doi:10.14359/19758.

[29] P. K. Mehta, Concrete Structure Properties and Materials, Englewood Cliffs, New Jersey, 1986.

[30] M. M. Johari, J. Brooks, S. Kabir, P. Rivard, Influence of supplementary cementitious materials on engineering properties of high strength concrete, Construction and Building Materials 25 (2011) 2639–2648. doi:10.1016/j.conbuildmat.2010.12.013.

[31] K.-H. Yang, J.-K. Song, K.-I. Song, Assessment of CO_2 reduction of alkali-activated concrete, Journal of Cleaner Production 39 (2013) 265–272. doi:10.1016/j.jclepro.2012.08.001.

[32] L. K. Turner, F. G. Collins, Carbon dioxide equivalent (CO2-e) emissions: A comparison between geopolymer and OPC cement concrete, Construction and Building Materials 43 (2013) 125–130. doi:10.1016/j.conbuildmat.2013.01.023.

[33] X. Gao, Q. Yu, H. Brouwers, Reaction kinetics, gel character and strength of ambient temperature cured alkali activated slag–fly ash blends, Construction and Building Materials 80 (2015) 105–115. doi:10.1016/j.conbuildmat.2015.01.065.

[34] M. Shojaei, K. Behfarnia, R. Mohebi, Application of alkali-activated slag concrete in railway sleepers, Materials & Design 69 (2015) 89–95. doi:10.1016/j.matdes.2014.12.051.

[35] A. Gholampour, T. Ozbakkaloglu, Performance of sustainable concretes containing very high volume class-f fly ash and ground granulated blast furnace slag, Journal of Cleaner Production 162 (2017) 1407–1417. doi:10.1016/j.jclepro.2017.06.087.

[36] A. M. Neville, Properties of Concrete: Fourth Edition, Longman, 1996.

[37] M. Heikal, H. El-Didamony, T. Sokkary, I. Ahmed, Behavior of composite cement pastes containing microsilica and fly ash at elevated temperature, Construction and Building Materials 38 (2013) 1180–1190. doi:10.1016/j.conbuildmat.2012.09.069.

[38] M. Saad, S. Abo-El-Enein, G. Hanna, M. Kotkata, Effect of temperature on physical and mechanical properties of concrete containing silica fume, Cement and Concrete Research 26 (1996) 669–675. doi:10.1016/s0008-8846(96)85002-2.

[39] Z. Li, J. Peng, B. Ma, Investigation of chloride diffusion for high-performance concrete containing fly ash, microsilica, and chemical admixtures, ACI Materials Journal 96 (1999) 391–396. doi:10.14359/638.

[40] M. I. Khan, Permeation of high performance concrete, Journal of Materials in Civil Engineering 15 (2003) 84–92. doi:10.1061/(asce)0899-1561(2003)15:1(84).

[41] D. P. Bentz, P. E. Stutzman, Evolution of porosity and calcium hydroxide in laboratory concretes containing silica fume, Cement and Concrete Research 24 (1994) 1044–1050. doi:10.1016/0008-8846(94)90027-2.

[42] D. Bentz, O. Jensen, A. Coats, F. Glasser, Influence of silica fume on diffusivity in cement-based materials, Cement and Concrete Research 30 (2000) 953–962. doi:10.1016/s0008-8846(00)00264-7.

[43] G. Golewski, T. Sadowski, An analysis of shear fracture toughness KIIc and microstructure in concretes containing fly-ash, Construction and Building Materials 51 (2014) 207–214. doi:10.1016/j.conbuildmat.2013.10.044.

[44] G. L. Golewski, Evaluation of morphology and size of cracks of the interfacial transition zone (ITZ) in concrete containing fly ash (FA), Journal of Hazardous Materials 357 (2018) 298–304. doi:10.1016/j.jhazmat.2018.06.016.

[45] M. Thomas, M. Shehata, S. Shashiprakash, D. Hopkins, K. Cail, Use of ternary cementitious systems containing silica fume and fly ash in concrete, Cement and Concrete Research 29 (1999) 1207–1214. doi:10.1016/s0008-8846(99)00096-4.

[46] K. Hwang, T. Noguchi, F. Tomosawa, Prediction model of compressive strength development of fly-ash concrete, Cement and Concrete Research 34 (2004) 2269–2276. doi:10.1016/j.cemconres.2004.04.009.

[47] J. M. Justice, K. E. Kurtis, Influence of metakaolin surface area on properties of cement-based materials, Journal of Materials in Civil Engineering 19 (2007) 762–771. doi:10.1061/(asce)0899-1561(2007)19:9(762).

[48] A. L. Velosa, F. Rocha, R. Veiga, Influence of chemical and mineralogical composition of metakaolin on mortar characteristics, Acta Geodynamica et Geomaterialia 153 (2009) 121–126.

[49] S. Wild, J. Khatib, Portlandite consumption in metakaolin cement pastes and mortars, Cement and Concrete Research 27 (1997) 137–146. doi:10.1016/s0008-8846(96)00187-1.

[50] S. Antiohos, K. Maganari, S. Tsimas, Evaluation of blends of high and low calcium fly ashes for use as supplementary cementing materials, Cement and Concrete Composites 27 (2005) 349–356. doi:10.1016/j.cemconcomp.2004.05.001.

[51] T. Song, I. Dumitru, B. Bornstein, Manufacturing ultra high performance concretes by silica fume, ultra fine fly ash and metakaolin addition, Journal of Materials Science and Engineering A 7. doi:10.17265/2161-6213/2017.5-6.003.

[52] J. J. Hughes, P. Trtik, Micro-mechanical properties of cement paste measured by depth-sensing nanoindentation: a preliminary correlation of physical properties with phase type, Materials Characterization 53 (2004) 223–231. doi:10.1016/j.matchar.2004.08.014.

[53] G. Constantinides, F. J. Ulm, The effect of two types of C-S-H on the elasticity of cement-based materials: Results from nanoindentation and micromechanical modeling, Cement and Concrete Research 34 (2004) 67–80. doi:10.1016/s0008-8846(03)00230-8.

[54] J. Němeček, V. Králík, J. Vondřejc, Micromechanical analysis of heterogeneous structural materials, Cement & Concrete Composites 36 (2013) 85–92. doi:j.cemconcomp.2012.06.015.

[55] B. Pichler, C. Hellmich, J. Eberhardsteiner, Spherical and acicular representation of hydrates in a micromechanical model for cement paste: prediction of early-age elasticity and strength, Acta Mechanica 203 (3) (2009) 137–162. doi:10.1007/s00707-008-0007-9.

[56] B. Pichler, C. Hellmich, Upscaling quasi-brittle strength of cement paste and mortar: A multi-scale engineering mechanics model, Cement and Concrete Research 41 (2011) 467–476. doi:10.1016/j.cemconres.2011.01.010.

[57] V. Nežerka, J. Zeman, J. Němeček, Micromechanics-based simulations of compressive and tensile testing on lime-based mortars, Mechanics of Materials 105 (2017) 49–60. doi:10.1016/j.mechmat.2016.11.011.

[58] V. Nežerka, V. Hrbek, Z. Prošek, M. Somr, P. Tesárek, J. Fládr, Micromechanical characterization and modeling of cement pastes containing waste marble powder, Journal of Cleaner Production 195 (2018) 1081–1090. doi:10.1016/j.jclepro.2018.05.284.

[59] L. M. Gitman, H. Askes, L. J. Sluys, Coupled-volume multi-scale modelling of quasi-brittle material, European Journal of Mechanics - A/Solids 27 (2007) 302–327.

[60] I. Gitman, H. Askes, L. Sluys, Coupled-volume multi-scale modelling of quasi-brittle material, European Journal of Mechanics - A/Solids 27 (2008) 302–327. doi:10.1016/j.euromechsol.2007.10.004.

[61] V. Nežerka, P. Tesárek, J. Zeman, Fracture-micromechanics based model of mortars susceptible to shrinkage, Key Engineering Materials 592–593 (2014) 189–192. doi:10.4028/www.scientific.net/kem.592-593.189.

[62] J. J. Zheng, Z. Q. Guo, X. F. Huang, P. Stroeven, L. J. Sluys, ITZ volume fraction in concrete with spheroidal aggregate particles and application: Part II. prediction of the chloride diffusivity of concrete, Magazine of Concrete Research 63 (2011) 483–491. doi:10.1680/macr.2011.63.7.483.

[63] K. Wu, H. Shi, L. Xu, G. Ye, G. D. Schutter, Microstructural characterization of ITZ in blended cement concretes and its relation to transport properties, Cement and Concrete Research 79 (2016) 243–256. doi:10.1016/j.cemconres.2015.09.018.

[64] Y. Gao, G. D. Schutter, G. Ye, J. Jiang, W. Sun, Assessment of structural feature and ionic diffusivity of ITZ in blended cementitious composites, Journal of Advanced Concrete Technology 14 (2016) 344–353. doi:10.3151/jact.14.344.

[65] European Committee for Standardization, EN 197-1:2011: Cement. Composition, specifications and conformity criteria for common cements., BSI, 2011.

[66] J. Fládr, P. Bílý, Analysis of hydration phase of cement pastes with partial replacement of cement by latent hydraulic additives, IOP Conference Series: Materials Science and Engineering 431 (2018) 052003. doi:10.1088/1757-899x/431/5/052003.

[67] W. Changlong, F. Weihua, Experimental study and application of HPC by mixing fly ash, in: 2009 Third International Symposium on Intelligent Information Technology Application Workshops, 2009. doi:10.1109/iitaw.2009.59.

[68] C. Cao, W. Sun, H. Qin, The analysis on strength and fly ash effect of roller-compacted concrete with high volume fly ash, Cement and Concrete Research 30 (2000) 71–75. doi:10.1016/s0008-8846(99)00203-3.

[69] Z. Yamei, S. Wei, S. Lianfei, Mechanical properties of high performance concrete made with high calcium high sulfate fly ash, Cement and Concrete Research 27 (1997) 1093–1098. doi:10.1016/s0008-8846(97)00087-2.

[70] R. Chylík, K. Šeps, Influence of cement replacement by admixture on mechanical properties of concrete, Proceedings of the 12th FIB PhD Symposium in Civil Engineering, Prague (2018) 1267–1274.

[71] C. Tam, D. S. Babu, W. Li, EN 206 conformity testing for concrete strength in compression, Procedia Engineering 171 (2017) 227–237. doi:10.1016/j.proeng.2017.01.330.

[72] BS EN 206-1:2013: Concrete. Specification, performance, production and conformity, British Standards Institution, London, 2013. doi:10.3403/30257890u.

[73] BS EN 480-11:2005: Admixtures for concrete, mortar and grout—Test methods—Part 11: Determination of air void characteristics in hardened concrete. doi:10.3403/30129094.

[74] B. K. Marsh, R. L. Day, Pozzolanic and cementitious reactions of fly ash in blended cement pastes, Cement and Concrete Research 18 (1988) 301–310. doi:10.1016/0008-8846(88)90014-2.

[75] V. Nežerka, Z. Slížková, P. Tesárek, T. Plachý, D. Frankeová, V. Petráňová, Comprehensive study on microstructure and mechanical properties of lime-pozzolan pastes, Cement and Concrete Research 64 (2014) 17–29. doi:10.1016/j.cemconres.2014.06.006.

[76] K. L. Scrivener, H. H. Patel, P. L. Pratt, L. J. Parrott, Analysis of phases in cement paste using backscattered electron images, methanol adsorption and thermogravimetric analysis, MRS Proceedings 85 (1986) 321–332. doi:10.1557/proc-85-67.

[77] V. Nežerka, J. Trejbal, Assessment of aggregate-bitumen coverage using entropy-based image segmentation, Road Materials and Pavement Design 0 (2019) 1–12. doi:10.1080/14680629.2019.1605304.

[78] J. Woirgard, J.-C. Dargenton, An alternative method for penetration depth determination in nanoindentation measurements, Journal of Materials Research 12 (1997) 2455–2458. doi:10.1557/jmr.1997.0324.

[79] A. Fischer-Cripps, A simple phenomenological approach to nanoindentation creep, Materials Science and Engineering: A 385 (2004) 74–82. doi:10.1016/j.msea.2004.04.070.

[80] P. Tesárek, T. Plachý, P. Ryparová, J. Němeček, Micromechanical properties of different materials on gypsum basis, Chemické listy 106 (2012) 547–548.

[81] W. C. Oliver, G. M. Pharr, An improved technique for determining hardness and elastic modulus using load and displacement sensing indentation experiments, Journal of Materials Research 7 (1992) 1564–1583. doi:10.1557/jmr.1992.1564.

[82] G. M. Pharr, A. Bolshakov, Understanding nanoindentation unloading curves, Journal of Materials Research 17 (2002) 2660–2671. doi:10.1557/jmr.2002.0386.

[83] S. Bhave, R. Eslami, M. Jacob, Sparse spectral deconvolution algorithm for noncartesian MR spectroscopic imaging, Magnetic Resonance in Medicine 71 (2013) 469–476. doi:10.1002/mrm.24693.

[84] J. C. C. Trujillo, J. M. M. Meza, Deconvolution of design parameters from elasto-plastic energy data acquired by nanoindentation in ceramic coatings, Scientia et technica 22 (2017) 131. doi:10.22517/23447214.12371.

[85] BS EN 12504-4:2004: Testing concrete. Determination of ultrasonic pulse velocity , British Standards Institution, London, 2004.

[86] BS EN 12390-3:2009: Testing hardened concrete Part 3: Compressive strength of test specimens, British Standards Institution, London, 2009. doi:10.3403/02508604u.

[87] P. Bílý, J. Fládr, R. Chylík, L. Vráblík, V. Hrbek, The effect of cement replacement and homogenization procedure on mechanical properties of high performance concrete, Magazine of Civil Engineering 84.

[88] J. Vorel, V. Šmilauer, Z. Bittnar, Multiscale simulations of concrete mechanical tests, Journal of Computational and Applied Mathematics 236 (2012) 4882–4892. doi:10.1016/j.cam.2012.01.009.

[89] T. Mori, K. Tanaka, Average stress in matrix and average elastic energy of materials with mixfitting inclusions, Acta Metallurgica 21 (1973) 571–574. doi:10.1016/0001-6160(73)90064-3.

[90] Y. Benveniste, A new approach to the application of Mori-Tanaka theory in composite materials, Mechanics of Materials 6 (1987) 147–157. doi:10.1016/0167-6636(87)90005-6.

[91] P. H. Feenstra, R. de Borst, Constitutive model for reinforced concrete, Journal of Engineering Mechanics, ASCE 121 (1995) 587–595. doi:10.1061/(asce)0733-9399(1995)121:5(587).

[92] M. François, A new yield criterion for the concrete materials, Comptes Rendus Mécanique 336 (2008) 417–421. doi:10.1016/j.crme.2008.01.010.

[93] J. Stránský, J. Vorel, J. Zeman, M. Šejnoha, Mori-Tanaka based estimates of effective thermal conductivity of various engineering materials, Micromachines 2 (2011) 129–149. arXiv:1101.4121.

[94] M. Königsberger, B. Pichler, C. Hellmich, Micromechanics of ITZ-aggregate interaction in concrete part i: Stress concentration, Journal of the American Ceramic Society 97 (2013) 535–542. doi:10.1111/jace.12591.

[95] M. Königsberger, B. Pichler, C. Hellmich, Micromechanics of ITZ-aggregate interaction in concrete part II: Strength upscaling, Journal of the American Ceramic Society 97 (2013) 543–551. doi:10.1111/jace.12606.

[96] V. Nežerka, J. Zeman, A micromechanics-based model for stiffness and strength estimation of cocciopesto mortars, Acta Polytechnica 52 (2012) 29–37.

[97] J. Huang, K. Krabbenhoft, A. Lyamin, Statistical homogenization of elastic properties of cement paste based on x-ray microtomography images, International Journal of Solids and Structures 50 (2013) 699–709. doi:10.1016/j.ijsolstr.2012.10.030.

[98] G. W. Milton, The Theory of Composites, Cambridge Monographs on Applied and Computational Mathematics, Cambridge University Press, 2002. doi:10.1115/1.1553445.

[99] J. D. Eshelby, The Determination of the Elastic Field of an Ellipsoidal Inclusion, and Related Problems, Proceedings of the Royal Society of London 241 (1957) 376–396. doi:10.1098/rspa.1957.0133.

[100] G. Constantinides, F.-J. Ulm, The nanogranular nature of c-s-h, Journal of the Mechanics and Physics of Solids 55 (2007) 64–90. doi:10.1016/j.conbuildmat.2016.12.189.

[101] O. Bernard, F.-J. Ulm, E. Lemarchand, A multiscale micromechanics-hydration model for the early-age elastic properties of cement-based materials, Cement and Concrete Research 33 (2003) 1293–1309. doi:10.1016/s0008-8846(03)00039-5.

[102] J. Sanahuja, L. Dormieux, G. Chanvillard, Modelling elasticity of a hydrating cement paste, Cement and Concrete Research 37 (2007) 1427–1439. doi:10.1016/j.cemconres.2007.07.003.

[103] L. Stefan, F. Benboudjema, J.-M. Torrenti, B. Bissonnette, Prediction of elastic properties of cement pastes at early ages, Computational Materials Science 47 (2010) 775–784. doi:10.1016/j.commatsci.2009.11.003.

[104] R. A. Schultz, Brittle strength of basaltic rock masses with applications to Venus, Journal of Geophysical Research 98 (1993) 10883. doi:10.1029/93je00691.

[105] J. A. Rossignolo, Effect of silica fume and SBR latex on the pasteaggregate interfacial transition zone, Materials Research 10 (2007) 83–86. doi:10.1590/s1516-14392007000100018.

[106] J. Branch, R. Epps, D. Kosson, The impact of carbonation on bulk and ITZ porosity in microconcrete materials with fly ash replacement, Cement and Concrete Research 103 (2018) 170–178. doi:10.1016/j.cemconres.2017.10.012.

[107] P. Duan, Z. Shui, W. Chen, C. Shen, Efficiency of mineral admixtures in concrete: Microstructure, compressive strength and stability of hydrate phases, Applied Clay Science 83-84 (2013) 115–121. doi:10.1016/j.clay.2013.08.021.

[108] Y. Gao, G. D. Schutter, G. Ye, H. Huang, Z. Tan, K. Wu, Characterization of ITZ in ternary blended cementitious composites: Experiment and simulation, Construction and Building Materials 41 (2013) 742–750. doi:10.1016/j.conbuildmat.2012.12.051.

[109] A. Bentur, M. D. Cohen, Effect of condensed silica fume on the microstructure of the interfacial zone in portland cement mortars, Journal of the American Ceramic Society 70 (1987) 738–743. doi:10.1111/j.1151-2916.1987.tb04873.x.

[110] D. Bentz, E. Garboczi, Simulation studies of the effects of mineral admixtures on the cement paste-aggregate interfacial zone, ACI Materials Journal 88 (1991) 518–529. doi:10.14359/2179.

[111] V. Paulon, D. D. Molin, P. Monteiro, Statistical analysis of the effect of mineral admixtures on the strength of the interfacial transition zone, Interface Science 12 (2004) 399–410. doi:10.1023/b:ints.0000042338.54460.02.

[112] A. Cwirzen, V. Penttala, Aggregate-cement paste transition zone properties affecting the salt-frost damage of high-performance concretes, Cement and Concrete Research 35 (2005) 671–679. doi:10.1016/j.cemconres.2004.06.009.